MIT Libraries | DSpace@MIT

MIT Open Access Articles

EPIC 219388192b—An Inhabitant of the Brown Dwarf Desert in the Ruprecht 147 Open Cluster

Massachusetts Institute of Technology

EPIC 219388192b—An Inhabitant of the Brown Dwarf Desert in the Ruprecht 147 Open Cluster

Grzegorz Nowak[1,2], Enric Palle[1,2], Davide Gandolfi[3,4], Fei Dai[5], Antonino F. Lanza[6], Teruyuki Hirano[7], Oscar Barragán[3], Akihiko Fukui[8], Hans Bruntt[9], Michael Endl[10], William D. Cochran[10], Pier G. Prada Moroni[11,12], Jorge Prieto-Arranz[1,2], Amanda Kiilerich[9], David Nespral[1,2], Artie P. Hatzes[13], Simon Albrecht[9], Hans Deeg[1,2], Joshua N. Winn[14], Liang Yu[5], Masayuki Kuzuhara[15,16], Sascha Grziwa[17], Alexis M. S. Smith[18], Eike W. Guenther[13], Vincent Van Eylen[19], Szilard Csizmadia[18], Malcolm Fridlund[20,21], Juan Cabrera[18], Philipp Eigmüller[18], Anders Erikson[18], Judith Korth[17], Norio Narita[15,16,22], Martin Pätzold[17], Heike Rauer[18,23], and Ignasi Ribas[24]

[1] Instituto de Astrofísica de Canarias (IAC), E-38205 La Laguna, Tenerife, Spain
[2] Departamento de Astrofísica, Universidad de La Laguna (ULL), E-38206 La Laguna, Tenerife, Spain
[3] Dipartimento di Fisica, Universitá di Torino, Via P. Giuria 1, I-10125, Torino, Italy
[4] Landessternwarte Königstuhl, Zentrum für Astronomie der Universität Heidelberg, Königstuhl 12, D-69117 Heidelberg, Germany
[5] Department of Physics and Kavli Institute for Astrophysics and Space Research,
Massachusetts Institute of Technology, Cambridge, MA 02139, USA
[6] INAF-Osservatorio Astrofisico di Catania, Via S. Sofia, 78-95123 Catania, Italy
[7] Department of Earth and Planetary Sciences, Tokyo Institute of Technology, 2-12-1 Ookayama, Meguro-ku, Tokyo 152-8551, Japan
[8] Okayama Astrophysical Observatory, National Astronomical Observatory of Japan, Asakuchi, Okayama 719-0232, Japan
[9] Stellar Astrophysics Centre, Department of Physics and Astronomy, Aarhus University, Ny Munkegade 120, DK-8000 Aarhus C, Denmark
[10] Department of Astronomy and McDonald Observatory, University of Texas at Austin,
2515 Speedway, Stop C1400, Austin, TX 78712, USA
[11] INFN, Section of Pisa, Largo Bruno Pontecorvo 3, I-56127, Pisa, Italy
[12] Department of Physics "E. Fermi,"University of Pisa, Largo Bruno Pontecorvo 3, I-56127, Pisa, Italy
[13] Thüringer Landessternwarte Tautenburg, Sternwarte 5, D-07778 Tautenburg, Germany
[14] Princeton University, Department of Astrophysical Sciences, 4 Ivy Lane, Princeton, NJ 08544 USA
[15] Astrobiology Center, National Institutes of Natural Sciences, 2-21-1 Osawa, Mitaka, Tokyo 181-8588, Japan
[16] National Astronomical Observatory of Japan, 2-21-1 Osawa, Mitaka, Tokyo 181-8588, Japan
[17] Rheinisches Institut für Umweltforschung an der Universität zu Köln, Aachener Strasse 209, D-50931 Köln, Germany
[18] Institute of Planetary Research, German Aerospace Center, Rutherfordstrasse 2, D-12489 Berlin, Germany
[19] Leiden Observatory, Leiden University, 2333CA Leiden, The Netherlands
[20] Leiden Observatory, University of Leiden, P.O. Box 9513, 2300 RA, Leiden, The Netherlands
[21] Department of Earth and Space Sciences, Chalmers University of Technology, Onsala Space Observatory, 439 92 Onsala, Sweden
[22] Department of Astronomy, The University of Tokyo, 7-3-1 Hongo, Bunkyo-ku, Tokyo 113-0033, Japan
[23] Center for Astronomy and Astrophysics, TU Berlin, Hardenbergstr. 36, D-10623 Berlin, Germany
[24] Institut de Ciències de l'Espai (CSIC-IEEC), Carrer de Can Magrans, Campus UAB, E-08193 Bellaterra, Spain

Abstract

We report the discovery of EPIC 219388192b, a transiting brown dwarf in a 5.3 day orbit around a member star of Ruprecht 147, the oldest nearby open cluster association, which was photometrically monitored by K2 during its Campaign 7. We combine the K2 time-series data with ground-based adaptive optics imaging and high-resolution spectroscopy to rule out false positive scenarios and determine the main parameters of the system. EPIC 219388192b has a radius of $R_b = 0.937 \pm 0.032$ R_{Jup} and mass of $M_b = 36.84 \pm 0.97$ M_{Jup}, yielding a mean density of 59.6 ± 7.6 g cm^{-3}. The host star is nearly a solar twin with mass $M_\star = 1.01 \pm 0.04$ $M_\odot$, radius $R_\star = 1.01 \pm 0.03$ $R_\odot$, effective temperature $T_{eff} = 5850 \pm 85$ K, and iron abundance [Fe/H] $= 0.03 \pm 0.08$ dex. Its age, spectroscopic distance, and reddening are consistent with those of Ruprecht 147, corroborating its cluster membership. EPIC 219388192b is the first mature brown dwarf with precise determinations of mass, radius, and age, and serves as benchmark for evolutionary models in the substellar regime.

Key words: brown dwarfs – stars: individual (EPIC 219388192) – techniques: photometric –
techniques: radial velocities – techniques: spectroscopic

1. Introduction

Currently, more than one thousand brown dwarfs (BDs) have been identified over the past 20 years, either isolated, in binary systems, or in orbit around more massive stars (see Skrzypek et al. 2016 and references therein, as well as the DwarfArchives[25]). In particular, the sample of BDs orbiting stars has increased in recent years, thanks to exoplanet radial velocity (RV) surveys. The RV method enables the determination of the companion's orbital parameters and minimum mass $m \sin i$.

Using the astrometric method, which allows the determination of the orbital inclination, the dynamical masses of several BDs have been measured (e.g., Reffert & Quirrenbach 2011; Wilson et al. 2016). Dynamical masses have also been measured for a dozen or more brown dwarf binaries (see, e.g., Table 1 in Béjar et al. 2011, pp. 48–59 and references therein). However, a model-independent and full characterization of the companion, i.e., the determination of its mass, radius, and hence mean density, is possible only for eclipsing systems.

The sample of eclipsing brown dwarfs with measured masses, radii, and densities known today contains 2 BD binaries—

[25] http://dwarfarchives.org
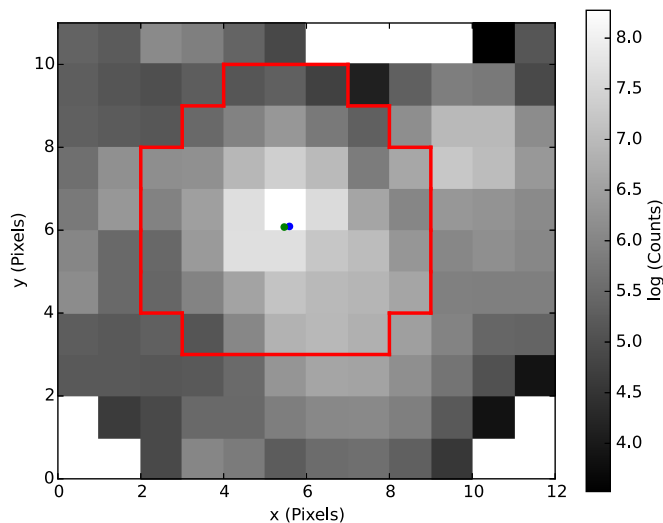
Figure 1. K2 image of EPIC 219388192 with a customized aperture shown in red and defined based on the amount of light of each pixel and level of background light. The intensity of shading indicates the electron count, going from high (light gray) to low (dark gray).

Figure 2. Detrended K2 light curve of EPIC 219388192. The equally spaced vertical solid red lines mark the position of each transit.

namely, 2MASS J053521840546085, an eclipsing binary system containing two extremely young brown dwarfs (Stassun et al. 2006) and EPIC 203868608b (David et al. 2016)—and 13 BDs that transit main-sequence (MS) stars. The full list of eclipsing brown dwarfs, including the first 11 BDs transiting MS stars, is given in Table 1 of Csizmadia (2016). The last two are the recently announced EPIC 201702477b (Bayliss et al. 2016) and EPIC 219388192b, the subjects of this work.

Here we present the discovery of the new eclipsing BD companion EPIC 219388192b, which was observed by the *Kepler* K2 space mission during its Campaign 7. The uniqueness of EPIC 219388192b stems from the fact that the host star is a member of the Ruprecht 147 cluster (Curtis et al. 2013), providing a robust age determination. Based on the spectroscopic, as well as near-infrared and optical photometric isochrone fitting to the Dartmouth (Dotter et al. 2008)[26] and PARSEC (Bressan et al. 2012)[27] stellar evolution models, Curtis et al. (2013) determined an age of 2.75–3.25 Gyr for the Ruprecht 147 cluster. Thus, EPIC 219388192b plays a very important role in the verification of the BD evolutionary models (Burrows et al. 1993, 1997, 2006, 2011; Chabrier et al. 2000; Baraffe et al. 2003; Saumon & Marley 2008).

The paper is organized as follows: in Section 2 we describe the K2 data analysis and the complementary observations from the ground. In Section 3 we describe the physical properties of the host star. In Section 4 we describe the joint analysis of the RV and photometric data. In Section 5 we describe the tidal evolution of the system, and in Section 6 we provide a discussion and summary of our results.

2. Observations and Data Reductions

2.1. K2 Photometry

EPIC 219388192 was a pre-selected target star of K2 Campaign 7, and together with the other 13,550 target stars, was observed from the 4th of October to the 26th of December
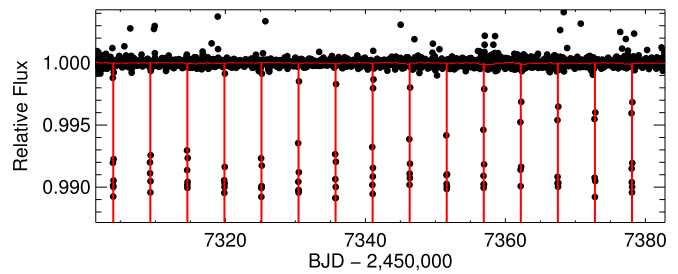
2015. Images of EPIC 219388192 were downloaded from the MAST archive[28] and used to produce a detrended K2 light curve as described in detail in Dai et al. (2017). The pixel mask used to perform simple aperture photometry is presented in Figure 1. After extracting the time-series data of all Field 7 targets, we searched the light curves for transiting planet candidates using the box-fitting least-squares (BLS) routine (Kovács et al. 2002; Jenkins et al. 2010) improved by implementing the optimal frequency sampling described in Ofir (2014). The ~1% deep transits of EPIC 219388192b were clearly detected with a signal-to-noise ratio (S/N) of 15.8 (defined as a peak signal over the local variance of the signal strength for each peak in the BLS spectrum). A linear ephemeris analysis gave a best-fit period of 5.292569 ± 0.000026 days and mid-time of the transit $T_{c,0} = 2457346.32942 \pm 0.00011$ (BJD$_{TDB}$). Figure 2 shows the detrended light curve of EPIC 219388192 with correction for centroid motions and baseline flux variations. The baseline flux variation was removed by spline fitting with a width of 3 days. The transit signals are marked with red lines. No secondary eclipses were detected. We placed an upper bound of 90 ppm for the secondary eclipse at 95% confidence level by fitting a secondary eclipse at the expected location predicted with the EPIC 219388192b eccentricity and argument of the pericenter derived from RVs. Table 3 reports the main identifiers of EPIC 219388192 along with its coordinates, optical and near-infrared magnitudes, and proper motion.

2.2. High Contrast Imaging

We acquired high-resolution, high contrast images of EPIC 219388192 to search for potential nearby stars and estimate the contamination factor arising from these sources. We performed adaptive optics (AO) observations of EPIC 219388192 on 2016 June 19 (UT) using the Subaru 188-elements Adaptive Optics system (AO188; Hayano et al. 2010) along with the Infrared Camera and Spectrograph (IRCS; Kobayashi et al. 2000). To search for faint nearby companions, we obtained *H*-band saturated images of EPIC 219388192 with five-point dithering and sidereal tracking. The exposure time was set to 15 s. The sequence was repeated three times to increase the S/N. For each dithering position, we also obtained unsaturated frames of EPIC 219388192 with individual exposures of 1.5 s for the flux calibration.

The 15 s exposure frames taken at four out of five dithering points reveal the presence of two faint objects south of EPIC 219388192. To recover these faint stars, we discarded the frames in which these fainter stars were out of the field of view
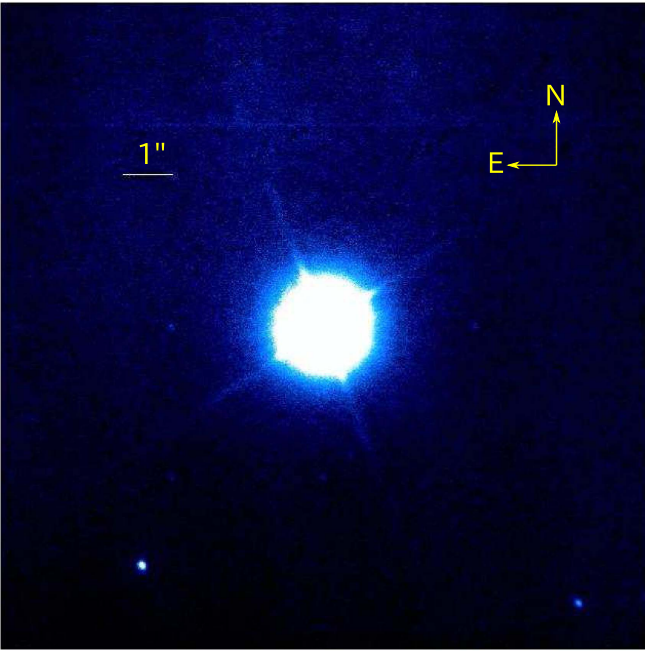
Figure 3. Combined saturated image of EPIC 219388192 obtained with the Subaru/IRCS+AO188 instrument with FOV of $13'' \times 13''$. The very faint sources at $2''$ away from the star visible east, west, south, and southeast are artifacts due to dithering.
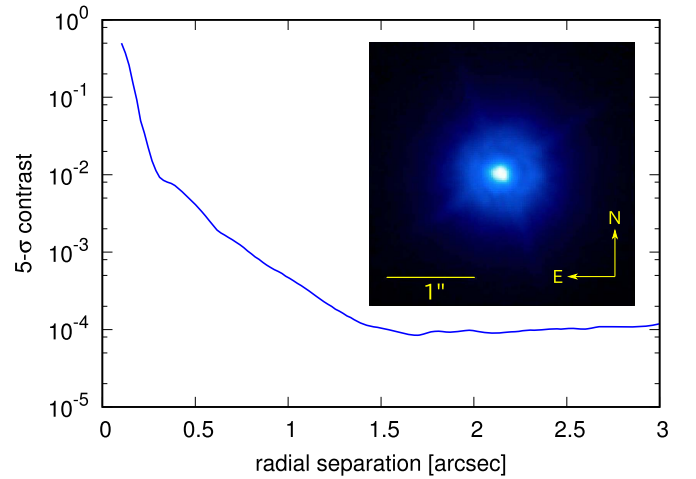
Table 1
Properties of Companion Candidates

Parameter	SE Object	SW Object
Separation ($''$)	5.998 ± 0.012	7.538 ± 0.015
Position Angle (deg)	142.740 ± 0.060	223.020 ± 0.050
Δm_H (mag)	7.087 ± 0.032	7.663 ± 0.057

(FOV). Therefore, the total exposure time for the saturated images used for the subsequent analysis is 180 s. On the other hand, these fainter stars were not visible in the 1.5 s exposure frames, and hence we simply combined all five unsaturated frames to measure the brightness of EPIC 219388192.

Each image was dark-subtracted and flat-fielded in a standard manner. After the image distortion on each frame was corrected, the 12 saturated and 5 unsaturated images were respectively aligned and median-combined to create the final combined images. The FWHMs of the stellar point-spread function on the saturated and unsaturated images are $0''.1$ and $0''.09$, respectively.

Figure 3 shows the combined saturated image of EPIC 219388192 with FOV of $13'' \times 13''$; the two faint stars are visible southwest (SW) and southeast (SE) of EPIC 219388192. Table 1 reports the separations, position angles, and Δm_H of these two objects. The flux contrasts of these stars to EPIC 219388192 ($<1.5 \times 10^{-3}$) are much smaller than the observed K2 transit depth ($\sim 1\%$), implying that those cannot be sources of false positive signals. We also checked the inner region ($<1''$) around EPIC 219388192 by visual inspection, but found no bright close-in companion (see the inset of Figure 4). Following Hirano et al. (2016), we drew the 5σ contrast curve as a function of the angular separation from EPIC 219388192, as shown in Figure 4.

Figure 4. 5σ contrast curve as a function of angular separation from EPIC 219388192. The inset displays the combined saturated image of the target with FOV of $3'' \times 3''$.

Table 2
FIES and Tull RVs, CCF Bisector Spans, and FWHMs

$\mathrm{BJD_{TDB}}$ $-2{,}450{,}000$	RV (m s^{-1})	σ_{RV} (m s^{-1})	BIS (m s^{-1})	FWHM (km s^{-1})
FIES				
7523.68062540	43713.500	32.663	15.5	12.999
7525.61496665	49737.784	19.656	17.5	13.006
7526.60509018	44979.980	18.852	-5.8	12.887
7527.60734381	42396.504	21.930	-13.0	12.975
7528.67908252	42872.233	9.904	-11.4	12.868
7535.69323565	50637.688	15.878	4.7	13.035
7566.63123022	46603.688	41.291	-8.5	12.796
7567.60778355	50686.232	15.100	-14.8	12.936
7568.52859679	46887.452	50.131	-67.5	12.949
Tull				
7543.80929600	41740.0	190.0	⋯	⋯
7608.75108000	45210.0	200.0	⋯	⋯
7609.70808000	49610.0	260.0	⋯	⋯

2.3. High Dispersion Spectroscopy

2.3.1. NOT/FIES

We started the RV follow-up of EPIC 219388192 using the FIber-fed Échelle Spectrograph (FIES; Frandsen & Lindberg 1999; Telting et al. 2014) mounted at the 2.56 m Nordic Optical Telescope (NOT) of the Roque de los Muchachos Observatory (La Palma, Spain). We took nine spectra between 2016 May and July as part of NOT observing programs P53-203, 53-109, and P53-016. We used the FIES high-resolution mode, which provides a resolving power of $R = 67{,}000$ in the spectral range 3700–7300 Å. Following the observing strategy described in Buchhave et al. (2010) and Gandolfi et al. (2015), we traced the RV drift of the instrument by acquiring long-exposed ThAr spectra ($T_{\mathrm{exp}} = 35$ s) immediately before and after each science exposure. The exposure time was set to 900–3600 s according to weather conditions and observing schedule constraints. The data reduction follows standard IRAF and IDL routines, which include bias subtraction, flat fielding, order tracing and extraction, and wavelength calibration. RV measurements were computed via multi-order

Table 3
Properties of EPIC 219388192

Parameter	Value	Source
Coordinates and Main Identifies		
R.A. 2000.0 (deg)	19:17:34.036	K2 EPIC
Decl. 2000.0 (deg)	−6:52:17.800	K2 EPIC
2MASS Identifier	19173402-1652177	2MASS PSC
UCAC Identifier	366-166973	UCAC4
Optical and Near-Infrared Magnitudes		
Kepler (mag)	12.336	K2 EPIC
B_J (mag)	13.284 ± 0.020	K2 EPIC
V_J (mag)	12.535 ± 0.020	K2 EPIC
g (mag)	12.854 ± 0.030	K2 EPIC
r (mag)	12.348 ± 0.020	K2 EPIC
i (mag)	12.348 ± 0.020	K2 EPIC
J (mag)	11.073 ± 0.023	K2 EPIC
H (mag)	10.734 ± 0.021	K2 EPIC
K (mag)	10.666 ± 0.021	K2 EPIC
Space Motion and Distance		
$PM_{R.A.}$ (mas yr^{-1})	-1.6 ± 2.5	PPMXL
$PM_{Decl.}$ (mas yr^{-1})	-31.9 ± 2.5	PPMXL
RV $_{\gamma,FIES}$ (m s^{-1})	45640 ± 10	This work
RV $_{\gamma,Tull}$ (m s^{-1})	45840 ± 120	This work
d (pc)	300 ± 18	This work
d (pc)	295 ± 15	1
Photospheric Parameters		
T_{eff} (K)	5850 ± 85	This work
$\log g_\star$ (dex)	4.38 ± 0.12	This work
[Fe/H] (dex)	0.03 ± 0.08	This work
Derived Physical Parameters		
$M_\star$ ($M_\odot$)	1.01 ± 0.04	This work
$R_\star$ ($R_\odot$)	1.01 ± 0.03	This work
Age(Gyr)	$3.6^{+1.8}_{-1.5}$	This work
Age (Gyr)	2.75—3.25	1
Stellar Rotation		
P_{rot} (days)	12.6 ± 2.10	This work
$v_{rot} \sin i_\star$ (km s^{-1})	4.1 ± 0.4	This work

Note. (1) From Curtis et al. (2013).

cross-correlations (CCF) with the RV-standard star HD 50692 (Udry et al. 1999) observed with the same instrument set-up as EPIC 219388192. The S/N per pixel at 5500 Å of the extracted spectra is in the range 15–35. Table 2 reports the FIES RVs, along with their 1σ error bars, CCF bisector spans (BS), and FWHMs. The RV errors were computed as the rms of 25 NOT/FIES spectral orders used for RV measurements. The FWHMs were measured from the Gaussian fit of the final CCF constructed by co-addition of CCFs from all orders used for RV measurements. Time stamps are given in Barycentric Julian Date in the Barycentric Dynamical Time (BJD$_{TDB}$; see, e.g., Eastman et al. 2010).

2.3.2. HJS/Tull

We also observed EPIC 219388192 with the Harlan J. Smith 2.7 m Telescope (HJS) and the Tull Coude Spectrograph (Tull et al. 1995) at McDonald Observatory (Fort Davis, TX). The Tull spectrograph covers the spectral range of 3400–10900 Å at a resolving power of $R = 60,000$. We obtained one spectrum

of the star in 2016 June and two spectra in 2016 August. We used exposures times of 1800 s, which resulted in an S/N between 35 and 49 per resolution element at 5650 Å. We calculated the absolute RV by cross-correlating the data with spectra of the RV-standard star HD 182488 (Udry et al. 1999), which we also observed in the same nights. Table 2 reports the extracted Tull RVs, along with their 1σ error bars, computed as the rms of the RVs of the 20 spectral orders used in the process of RV measurements.

3. Properties of the Host Star

3.1. Atmospheric and Physical Parameters

We determined the photospheric parameters of EPIC 219388192 from the co-added NOT/FIES spectra. The spectral analysis was performed with the versatile wavelength analysis VWA package[29] (Bruntt et al. 2012). The VWA iteratively fits abundances typically for 600–1000 spectral lines, individually for each line. The software uses atomic data from the VALD database (Kupka et al. 1999), which is a collection from many different sources. To fit the stellar photospheric parameters from measured abundances VWA uses 1D LTE atmosphere models interpolated in grids, either from the MARCS[30] (Gustafsson et al. 2008) or modified ATLAS9 models (Heiter et al. 2002). We measured an effective temperature $T_{eff} = 5850 \pm 85$ K, surface gravity $\log g_\star = 4.38 \pm 0.12$ (cgs), and iron abundance [Fe/H] $= 0.03 \pm 0.08$ dex. The $v_{rot} \sin i_\star$ was determined by artificially broadening the best-fit synthetic template using progressively increasing values of $v_{rot} \sin i_\star$ and by fitting it to the observed spectrum. For a given $v_{rot} \sin i_\star$, we convolved the model spectrum with a 1D kernel following the prescription given in Gray (1992) and using an IDL Astronomy User's Library macro.[31] We adopted a macroturbulent velocity $v_{mac} = 3.4 \pm 0.6$ km s^{-1} (Doyle et al. 2014) and measured a projected rotational velocity $v_{rot} \sin i_\star = 4.1 \pm 0.4$ km s^{-1} by fitting the profile of many isolated and unblended metal lines.

The stellar mass, radius, and age were derived by combining T_{eff} and [Fe/H] with the mean density $\rho_\star$ obtained from the joint analysis of the K2 transit light curves and NOT/FIES and HJS/ Tull RV measurements that take into account the non-zero eccentricity of EPIC 219388192b (Section 4). We compared the position of EPIC 219388192 on a $\rho_\star$ versus T_{eff} plot with a grid of evolutionary tracks computed ad hoc for this work by means of the FRANEC code (Tognelli et al. 2011). We used the same input physics and parameters adopted to build the Pisa Stellar Evolution Data Base for low-mass stars[32] and described in detail in Dell'Omodarme et al. (2012). The mixing-length parameter is $\alpha_{ml} = 1.74$, which is the FRANEC solar calibrated value for the heavy-element mixture of the Sun by Asplund et al. (2009). The models take into account microscopic diffusion by means of the routine developed by Thoul et al. (1994). We computed evolutionary tracks for various couples of initial metallicity Z and helium abundance Y, namely (0.015, 0.2790), (0.016, 0.2800), and (0.017, 0.2820). For each chemical composition, we followed the evolution from the pre-main-sequence phase to the beginning of the red giant phase for stars in the mass range $M = 0.90$–$1.10\ M_\odot$ with steps of $0.01\ M_\odot$.

---

[29] Available at https://sites.google.com/site/vikingpowersoftware/home.
[30] Available at http://marcs.astro.uu.se/.
[31] Available at http://idlastro.gsfc.nasa.gov/ftp/pro/astro/lsf_rotate.pro.
[32] Available at http://astro.df.unipi.it/stellar-models/.
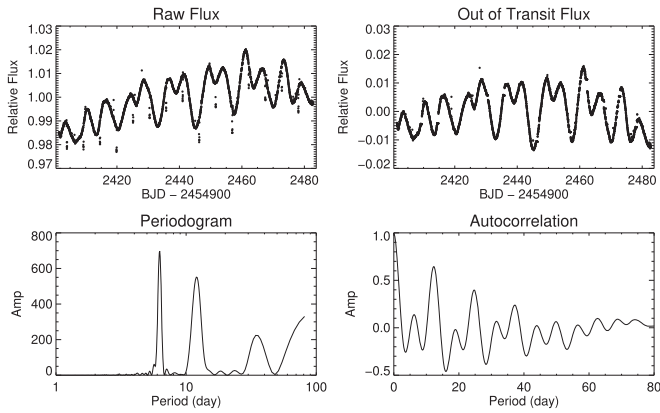
Figure 5. Upper left: raw flux of EPIC 219388192 processed with a modified algorithm that better preserves stellar activity. Upper right: smoothly joined flux used for computing the Lomb–Scargle periodogram (bottom-left panel) and auto cross-correlation function (bottom-right panel).

With a mass of $M_\star = 1.01 \pm 0.04\ M_\odot$ and radius of $R_\star = 1.01 \pm 0.03\ R_\odot$, EPIC 219388192 is a Sun-like star. Stellar mass and radius imply a surface gravity of $\log g_\star = 4.43 \pm 0.02$ (cgs), which agrees within 1σ with the value of $\log g_\star = 4.38 \pm 0.12$ (cgs) derived from the NOT/FIES co-added spectra. We estimated an age of $3.6^{+1.8}_{-1.5}$ Gyr, which is consistent with the Ruprecht 147 cluster's age of 2.75–3.25 Gyr determined by Curtis et al. (2013).

We derived the interstellar extinction (A_V) and distance (d) to the star following the technique outlined in Gandolfi et al. (2008). Briefly, we fitted the magnitudes encompassed by the spectral energy distribution of the star to synthetic magnitudes extracted from the NEXTGEN model spectrum (Hauschildt et al. 1999) with the same photospheric parameters as EPIC 219388192. We adopted the extinction law of Cardelli et al. (1989) and assumed a normal total-to-selective extinction value of $R_v = 3.1$. We derived a reddening of $A_V = 0.35 \pm 0.05$ mag, which is consistent with the Ruprecht 147 cluster's extinction $A_V = 0.25 \pm 0.05$ measured by Curtis et al. (2013). Assuming a black body emission at the star's effective temperature and radius, we measured a spectroscopic distance of EPIC 219388192 of $d = 300 \pm 18$ pc, which is also in excellent agreement with the cluster's distance ($d = 295 \pm 15$ pc; Curtis et al. 2013).

3.2. Stellar Rotation and Activity

The light curve of EPIC 219388192 displays periodic and quasi-periodic variations with a peak-to-peak photometric variation of about 2%. Given the spectral type of the star, the observed variability is very likely ascribable to active regions (spots and faculae) carried around by stellar rotation. This is corroborated by the detection of emission components in the Ca H & K lines. We measured the rotation period ($P_{\rm rot}$) of EPIC 219388192 using the auto-correlation function (ACF) method (McQuillan et al. 2014) applied to the out-of-transit light curve processed with a modified algorithm that better preserves stellar activity (Figure 5). The ACF displays correlation peaks separated by ~6.3 days, with a dominant peak at ~12.6 days (Figure 5). A visual inspection of the light curve reveals that features repeat every 12.6 days, suggesting that the latter is the rotation period of the star. The peaks occurring every 6.3 days are due to correlations between active regions at opposite stellar longitudes. We estimated a rotation

period and uncertainty of $P_{\rm rot} = 12.6 \pm 2.1$ days defined as the position and the FWHM of the strongest peak in the ACF. The Lomb–Scargle periodogram also shows a significant peak at both the rotation period of the star and its first harmonic, corroborating our findings (Figure 5).

Our estimate of the projected rotational velocity ($v_{\rm rot} \sin i_\star = 4.1 \pm 0.4\ {\rm km\ s^{-1}}$; Section 3.1) agrees with the equatorial velocity $v_{\rm rot} = 2\pi R_\star / P_{\rm rot} = 4 \pm 1\ {\rm km\ s^{-1}}$ computed from the stellar radius $R_\star$ and rotation period $P_{\rm rot}$. Using the rotation–activity–age relation proposed by Barnes (2007) with the above-determined stellar rotation period and adopting $(B - V)_0 = 0.642 \pm 0.016$ for Sun-like stars (Holmberg et al. 2006) we estimated a gyrochronological age of 1.12 ± 0.62 Gyr for EPIC 219388192. This estimate suggests that the rotation period of the star has been modified by some external action. In Section 5, we show that tides can be responsible.

3.3. Faint AO Companions

In Section 2.2 we present the detection of two faint stars close to EPIC 219388192. If we assume that the two objects are members of Ruprecht 147, we can obtain further information on these stars. Adopting the cluster's distance of 295 ± 15 pc, the angular separations imply a distance of 1769 ± 90 au (SE object) and 2224 ± 113 au (SW object) between EPIC 219388192 and the two sources. The apparent magnitude $m_H = 10.734 \pm 0.021$ mag of EPIC 219388192 yields an absolute magnitude of $M_H = 3.38 \pm 0.11$ mag. Thus, the magnitude differences listed in Table 1 translate into absolute magnitudes of $M_H = 10.47 \pm 0.12$ mag (SE object) and $M_H = 11.05 \pm 0.13$ mag (SW object). According to the Dartmouth isochrone table (Dotter et al. 2008), such faint stars ($M_H > 10$ mag) would be very late-type M dwarfs (later than M8) or brown dwarfs, with their masses being less than $\sim0.1\ M_\odot$. It would be of great interest if such multiple late-type stars, including EPIC 219388192b, are clustered within a relatively small region. Further observations (e.g., adaptive optics imaging in different bands) are required to verify the memberships of those faint objects.

3.4. Ruprecht 147 Cluster Membership

The EPIC 219388192's membership probability to the Ruprecht 147 cluster was reported by Curtis et al. (2013) as "possible." This was motivated by the RV of EPIC 219388192 measured by the authors to be $47.3\ {\rm km\ s^{-1}}$. This value is $\sim6\ {\rm km\ s^{-1}}$ higher than the cluster's average RV, $40.86 \pm 0.56\ {\rm km\ s^{-1}}$, which was determined by Curtis et al. (2013) based on the RV measurements of six known cluster members. The systemic velocity of EPIC 219388192 as measured using the NOT/FIES and HJS/Tull spectra is equal to $45.640 \pm 0.010\ {\rm km\ s^{-1}}$ and $45.840 \pm 0.120\ {\rm km\ s^{-1}}$, respectively, i.e., $\sim2\ {\rm km\ s^{-1}}$ lower than the value measured by Curtis et al. (2013). One possible reason of this discrepancy is the high K semi-amplitude of EPIC 219388192b ($\sim4.25\ {\rm km\ s^{-1}}$). Unfortunately, Curtis et al. (2013) does not provide the epoch of EPIC 219388192b RV measurement obtained with the 3 m Shane/Hamilton instrument and presented in their Table 3 ($47.3\ {\rm km\ s^{-1}}$). Taking into account the mean value of EPIC 219388192b systemic velocity ($RV_\gamma \sim 45.75\ {\rm km\ s^{-1}}$) and the eccentricity, its redial velocity may be as high as $50.75\ {\rm km\ s^{-1}}$ (see the phase-folded RV curve presented in Figure 7). The RV value presented by

Table 4
Results from the Global Fit of the Photometric and
Spectroscopic Data of EPIC 219388192

Parameter	Value
Fitted Parameters	
Orbital period P_{orb} (days)	5.292569 ± 0.000026
Epoch of the transit $T_{0,b}$ (BJD$_{TDB}$)	$2457346.32942 \pm 0.00011$
Scaled radius $R_b/R_\star$	0.09321 ± 0.00046
Scaled semimajor axis $a/R_\star$	$12.62^{+0.10}_{-0.15}$
Orbit inclination i (degrees)	90.0 ± 0.7
Impact parameter b	0.00 ± 0.15
Linear limb darkening coefficient u_1	0.468 ± 0.040
Quadratic limb darkening coefficient u_2	0.013 ± 0.087
Orbit eccentricity e	0.1929 ± 0.0019
Stellar argument of periastron ω	345.9 ± 1.0
RV semi-amplitude variation K (m s^{-1})	4267 ± 12
Systemic velocity γ_{FIES} (m s^{-1})	45640 ± 10
Systemic velocity γ_{Tull} (m s^{-1})	45840 ± 120
RV jitter σ_j (m s^{-1})	9^{+13}_{-6}
Derived Parameters	
Brown dwarf mass M_b (M_{Jup})	36.84 ± 0.97
Brown dwarf radius R_b (R_{Jup})	0.937 ± 0.032
Brown dwarf mean density ρ_b (g cm^{-3})	59.6 ± 7.6
Brown dwarf equilibrium temperature (K)[1]	1164 ± 40
Semimajor axis a (au)	0.0593 ± 0.0029
Host star mean density $\rho_\star$ (g cm^{-3})	1.369 ± 0.056

Note. (1) Assuming isotropic reradiation and a Bond albedo of zero.
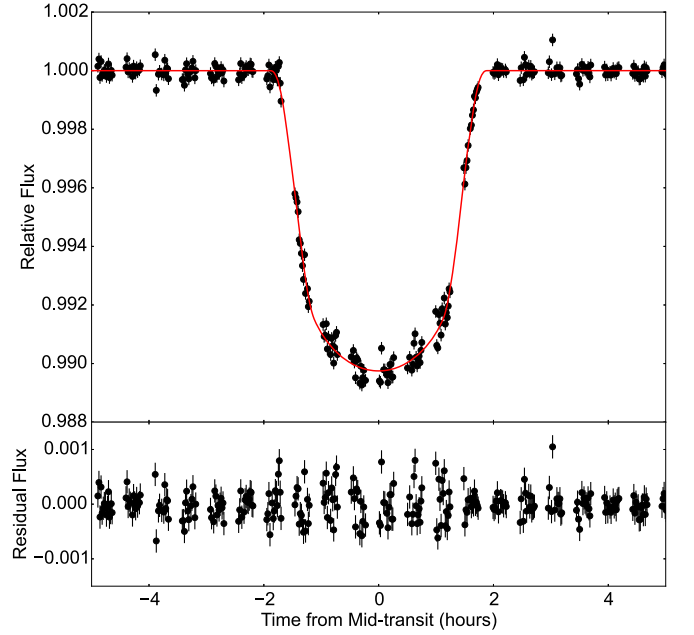
Curtis et al. (2013) is therefore in agreement with our measurements. Our determination of the EPIC 219388192b systemic velocity, although higher than the typical cluster RV of 40.86 ± 0.56 km s^{-1}, is within the 39–47 km s^{-1} range of the 3 m Shane/Hamilton RVs for the highest confidence members of Ruprecht 147 cluster (see Table 4 of Curtis et al. 2013). The other reason for the difference between our determination of the EPIC 219388192b systemic velocity and the typical cluster RV of 40.86 ± 0.56 km s^{-1} found by Curtis et al. (2013) as well as between the other instrument RV ranges for the highest quality cluster members presented in their Table 4 may be the systematic shifts of the RV offsets between different spectrographs (see a detailed discussion of these effects in Sections 2.2.3, 2.3, and 2.4 of Curtis et al. 2013).

Curtis et al. (2013) defined the high confidence Ruprecht 147 cluster members as those with the radial distance in proper motion space (r_{PM}) below 5 mas yr^{-1} from the cluster mean value ((PM$_{R.A.}$, PM$_{Decl.}$) = $(-1.1, -27.3)$ mas yr^{-1}). With the proper motions from the PPMXL catalog[33] (Roeser et al. 2010) ((PM$_{R.A.}$, PM$_{Decl.}$) = $(-1.6 \pm 2.5, -31.9 \pm 2.5)$ mas yr^{-1}), which gave $r_{PM} = 4.6 \pm 2.8$ mas yr^{-1}, EPIC 219388192 is the highest confidence member of Ruprecht 147 cluster. With the proper motions listed in the K2 Ecliptic Plane Input Catalog (EPIC)[34] (Huber et al. 2016) and taken from the UCAC4 catalog[35] (Zacharias et al. 2013) ((PM$_{R.A.}$, PM$_{Decl.}$) = $(-1.2 \pm 1.4, -21.6 \pm 3.4)$ mas yr^{-1}), $r_{PM} = 5.7 \pm 3.5$ mas yr^{-1}. Although

[33] Available at http://vizier.u-strasbg.fr/viz-bin/VizieR?-source=I/317&-to=3.
[34] Available at https://archive.stsci.edu/k2/epic/search.php.
[35] Available at http://vizier.u-strasbg.fr/viz-bin/VizieR?-source=I/322A&-to=3.

Figure 6. Upper panel: EPIC 219388192's transit light curves folded to the orbital period of the planet and best-fitting transit model (red line). Lower panel: residuals to the fit.

the above value of the radial distance in proper motion space is higher than the threshold chosen by Curtis et al. (2013), it meets the condition within the error bars.

Our estimates of the distance, reddening, and age of EPIC 219388192 (Section 3.1) are all consistent with those of Ruprecht 147. We conclude that there is now solid evidence for the star being a member of the Ruprecht 147 cluster.

4. Global Analysis

To estimate the system parameters, we performed a global joint analysis of the K2 transit light curves and the NOT/FIES and HJS/Tull RV measurements using the following χ^2 statistic:

$$\chi^2 = \sum_{i=1}^{i=N_f} \frac{(f_{obs,i} - f_{mod,i})^2}{\sigma^2_{f,i}}$$
$$+ \sum_{i=1}^{i=N_{FIES,RV}} \frac{(RV_{FIES,obs,i} - RV_{FIES,mod,i})^2}{\sigma^2_{FIES,RV,i}}$$
$$+ \sum_{i=1}^{i=N_{Tull,RV}} \frac{(RV_{Tull,obs,i} - RV_{Tull,mod,i})^2}{\sigma^2_{Tull,RV,i}}, \quad (1)$$

where N_f, $N_{FIES,RV}$, and $N_{Tull,RV}$ are the number of the K2 photometric, NOT/FIES, and HJS/Tull RV measurements, respectively, and $f_{obs,i}$, $RV_{FIES,obs,i}$, and $RV_{Tull,obs,i}$ are the ith observed K2 flux, NOT/FIES, and HJS/Tull RVs, and finally $\sigma_{f,i}$, $\sigma_{FIES,RV,i}$, and $\sigma_{Tull,RV,i}$ are their errors. For the RV model we adopted the following equations:

$$RV_{FIES,mod,i} = K [\cos(\nu + \omega) + e\cos(\omega)] + \gamma_{FIES}, \quad (2)$$

$$RV_{Tull,mod,i} = K [\cos(\nu + \omega) + e\cos(\omega)] + \gamma_{Tull}, \quad (3)$$

where K is the RV semi-amplitude, ν is the true anomaly, ω is the argument of periastron, e is the eccentricity, γ_{FIES} is the systemic velocity as measured from the NOT/FIES RV
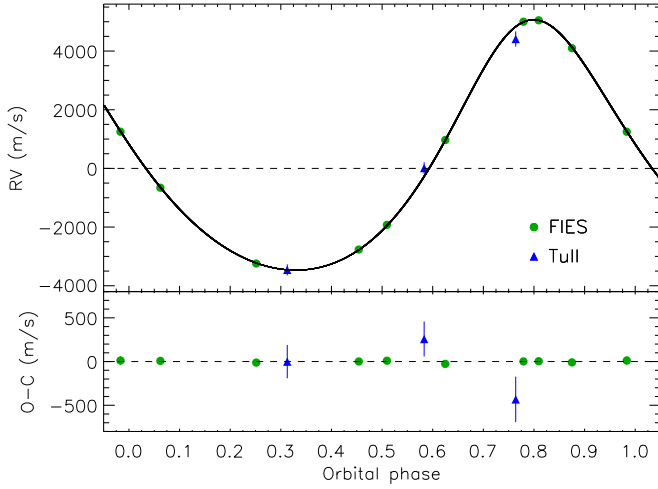
Figure 7. Upper panel. Phase-folded FIES (green circles) and Tull (blue triangles) RVs of EPIC 219388192 and best-fitting Keplerian model (thick line). Lower panel. RV residuals to the fit.

measurements, and γ_{Tull} is the systemic velocity as measured from the HJS/Tull RV measurements. For the transit model, we used the Python package BATMAN (Kreidberg 2015) to calculate the light curve.

There are four global parameters in our joint fit: time of conjunction (T_c), orbital period (P_{orb}), eccentricity (e), and argument of pericenter (ω). To avoid the bias toward non-zero eccentricity (Lucy & Sweeney 1971), we transformed e and ω to $\sqrt{e}\cos\omega$ and $\sqrt{e}\sin\omega$ during the fitting. There are five additional parameters involved in producing the light curve: the cosine of orbital inclination ($\cos i$), radius ratio ($R_b/R_\star$), semimajor axis in units of stellar radius ($a/R_\star$), and the quadratic limb darkening coefficients (u_1 and u_2). In the Keplerian model, we fit the stellar jitter (σ_j). Uniform priors were adopted for all parameters.

We first obtained the best-fit solution using the Levenberg–Marquart algorithm as implemented in the lmfit package in Python. To obtain the uncertainties and covariances on various parameters, we performed an MCMC analysis using the Python package emcee (Foreman-Mackey et al. 2013). We started 250 walkers drawn from a Gaussian distribution in parameter space, centered on the minimum-χ^2 solution. We stopped the walkers after 5000 links. We then checked the convergence by calculating the Gelman–Rubin potential scale reduction factor (Gelman & Rubin 1992) dropped below 1.02. We reported the median and the 16% and 84% percentiles of the marginalized posterior distribution for each parameters in Table 4. The observed data along with the best-fit models are displayed in Figures 6–7, for the phase-folded K2 light curve and orbital RVs, respectively. To check our results, we also modeled the data with the code pyaneti (O. Barragán et al. 2017, in preparation), a full MCMC Python/Fortran software. Following the strategy presented in Barragán et al. (2016), we sampled a wide range of the parameter space with 500 independent chains and took the final parameters from the final posterior distribution of the global minimum. The parameter estimates are in agreement well within 1σ.

The joint analysis allows the orbital configuration to be constrained to high precision. The orbit is relatively eccentric, $e = 0.1929 \pm 0.0019$. The joint analysis also derived a stellar density of 0.97 ± 0.04 solar density. The residual fluxes within
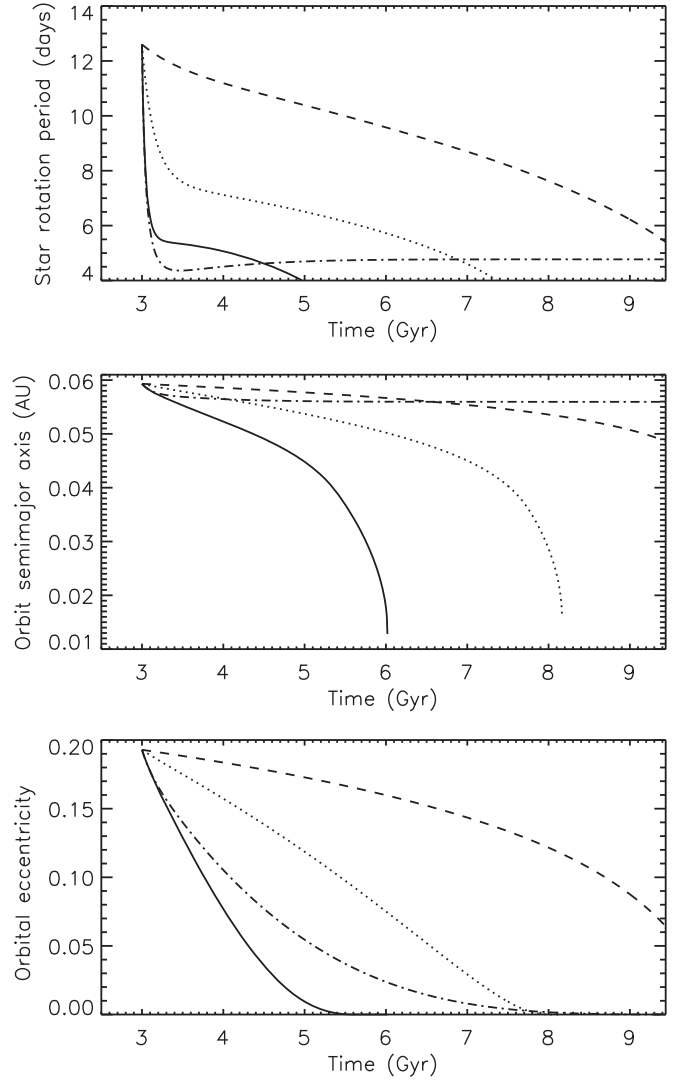

Figure 8. Upper panel: evolution of the stellar rotation period for $Q'_\star = 2.0 \times 10^6$ (solid line), $Q'_\star = 10^7$ (dotted line), and $Q'_\star = 5 \times 10^7$ (dashed line); the case without wind braking and $Q'_\star = 2 \times 10^6$ is also shown for comparison (dashed–dotted line). Middle panel: as in the upper panel, for the evolution of the orbital semimajor axis. Lower panel: as in the upper panel, for the evolution of the eccentricity.

the transit window show a larger scatter than those out of the transit window. We interpret this as the result of spot-crossing anomalies: when the brown dwarf occults a star spot during a transit, the planet occults a dimmer part of the stellar photosphere and therefore the observed flux will be higher than expected.

Mazeh et al. (2015) proposed the method to distinguish between prograde and retrograde planetary motion with respect to the stellar rotation using the transit timing variations (TTVs) induced by stellar spots. Following the above method, we checked for any sign of correlation between the TTV and the local slope of the flux variation of each transit. We detected a negative correlation with a Pearson correlation coefficient of -0.368. According to Mazeh et al. (2015), a negative correlation is indicative of a prograde orbit. The relatively large p-value of 0.177 does not allow the above negative correlation to be treated as a robust detection of prograde orbit, however. The overall amplitude of the Rossiter–McLaughlin effect, estimated using Equation (6) of Gaudi & Winn (2007) is
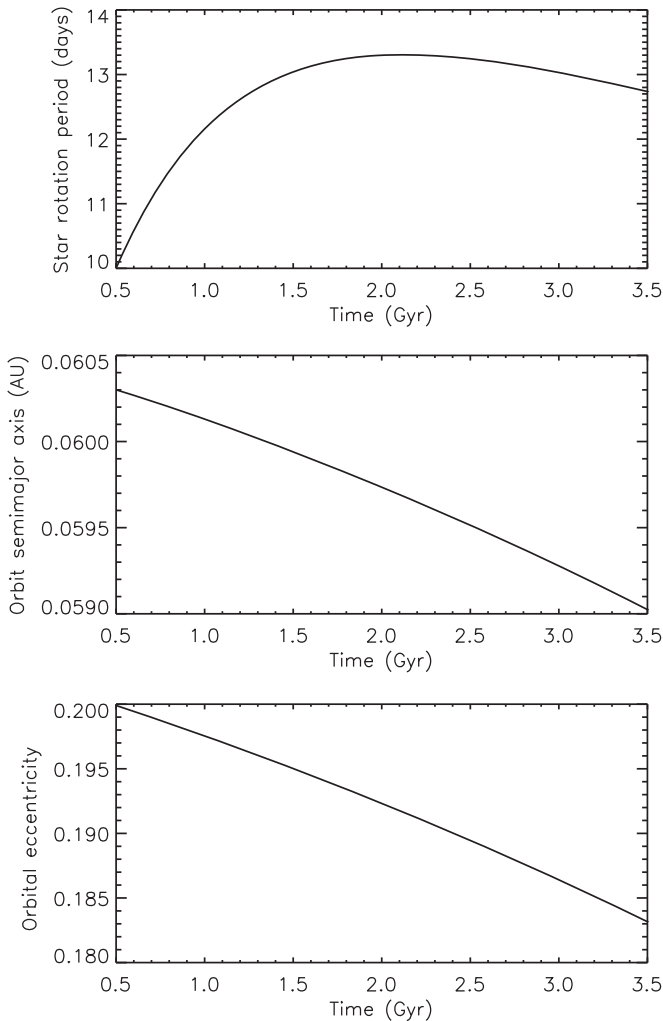
Figure 9. Same as Figure 8, but assuming a rotation period of 10 days when the star had an age of 500 Myr and $Q'_\star = 7 \times 10^7$.

equal to $36 \pm 9\ \mathrm{m\ s^{-1}}$. Taking into account the transit duration of EPIC 219388192b (3 hr) and the brightness of the host star ($V = 12.54$ mag), the transit spectroscopic measurements, using current and upcoming spectrographs installed on the 8–10 m class telescopes, should allow planetary motion with respect to the stellar rotation to be firmly determined.

5. Tidal Evolution of the System

EPIC 219388192 is an interesting system in which to study tidal interactions between a brown dwarf and a main-sequence star. Assuming that the modified tidal quality factors of the star and the brown dwarf are similar (see below), most of the tidal kinetic energy is dissipated inside the star rather than inside the brown dwarf because the ratio $\eta \equiv (\rho_b/\rho_\star)^2 (R_b/R_\star) \simeq 157.5 \gg 1$ (cf. Ogilvie 2014). The ratio ζ of the present orbital angular momentum to the stellar spin angular momentum is $\zeta \sim 150$ assuming a gyration radius of the star equal to that of the Sun at an age of 3 Gyr, i.e., $\beta = 0.289$ (Claret 2004). This implies that the tidal evolution of the stellar spin proceeds remarkably faster than that of the orbit with a transfer of angular momentum from the orbit to the stellar rotation because $P_{\rm rot} > P_{\rm orb}$ (Ogilvie 2014). Indeed, we find that the rotation period of the star $P_{\rm rot}$ is significantly shorter than

expected on the basis of gyrochronology because, by applying Equation (3) of Barnes (2007), we estimate a rotation period of $\sim$18.7 days for a single Sun-like star of $\sim$3 Gyr of age.

A preliminary model of the tidal evolution of the system is computed according to the approach of Leconte et al. (2010) which we modify by considering constant modified tidal quality factors for the star and the brown dwarf indicated with $Q'_\star$ and Q'_b, respectively. They are related to the constant time lag of the tides inside the corresponding body by means of Equation (19) of Leconte et al. (2010). Note that a smaller value of Q' implies a higher dissipation rate of the tidal energy inside the body. Moreover, we add the angular momentum loss produced by the stellar magnetized wind by considering a Skumanich-type law with saturation at an angular velocity equal to eight times that of the present Sun (e.g., Equation (2) in Spada et al. 2011) and assume a rigidly rotating star, the radius of which changes in time according to a 1 $M_\odot$ model (Dell'Omodarme et al. 2012).

The evolution of the system parameters is plotted in Figure 8 for different values of $Q'_\star$ ranging from 2.0×10^6 to 5×10^7; for comparison, we also plot the evolution for $Q'_\star = 2.0 \times 10^6$ without any wind braking. The orbital angular momentum and the stellar spin are assumed to be aligned with a present age of the system of 3 Gyr. The current ratio of the stellar rotation period to the orbital period is close but still above the critical value $P_{\rm rot}/P_{\rm orb} = 2$ for the excitation of inertial waves inside the star that would remarkably increase tidal dissipation (Ogilvie & Lin 2007). Since the star is spun up by tides, the critical value for the excitation of those waves is predicted to be reached within the next few hundred Myr for $Q' \leqslant 10^7$, while $\sim$2 Gyr will be required for $Q'_\star = 5 \times 10^7$ due to the slower acceleration of the stellar rotation. Beyond that threshold, the value of $Q'_\star$ will remarkably decrease accelerating the tidal evolution. In our constant-Q' approximation, this would favor the model computed with the smallest value of $Q'_\star$ with a fast spin-up of the star followed by the orbital decay of the system within $\approx$3 Gyr. The spin evolution is faster than the orbital decay because $\zeta \gg 1$. If the wind braking were absent, the system would avoid the orbital decay with the star reaching synchronization at a rotation period of $\sim$4.7 days and the orbit becoming circular with only a slight decrease of the semimajor axis, thanks to the large reservoir of angular momentum in the present orbit. The decay of the system is therefore a consequence of the magnetic wind braking with a phase of reduced acceleration of the stellar spin when the tidal spin-up and the wind loss temporarily balance with each other (Damiani & Lanza 2015). The increase of the stellar radius along the main sequence increases slightly the synchronization period, but does not affect our results.

The past evolution of the system is much more uncertain because we have no idea of its initial conditions. We may assume that the tidal interaction was not strong in the past because the rotation period of the star was too long for the excitation of inertial waves. As an illustrative model, we plot in Figure 9 the evolution with $Q' = 7 \times 10^7$ and a rotation period of 10 days at the age of 500 Myr when our model assuming rigid internal rotation becomes applicable. This is the typical rotation period of slowly rotating single stars of 1 $M_\odot$ in an open cluster of that age (cf. Gallet & Bouvier 2015). We see that the wind braking is initially stronger than the tidal spin-up, but when the star reaches an age of $\sim$2 Gyr, the tidal torque
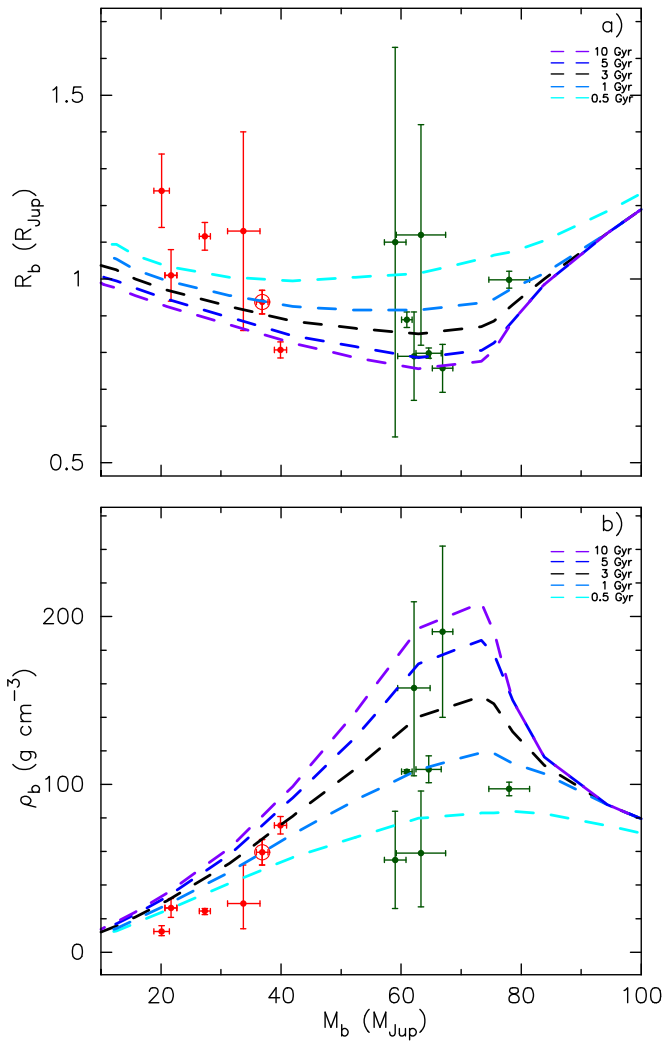
Figure 10. Mass–radius (a) and mass–density (b) relationships for all BDs transiting MS stars. The red filled circles indicate BDs with masses below $45\ M_{\mathrm{Jup}}$ at which Ma & Ge (2014) report a gap in the mass distribution. The dark-green filled circles indicate brown dwarfs with masses above $45\ M_{\mathrm{Jup}}$. EPIC 219388192b is indicated as a red filled circle with a rim. The dashed lines indicate the COND03 model radii and densities for BDs of 10 Gyr (violet), 5 Gyr (blue), 3 Gyr (black), 1 Gyr (light-blue), and 0.5 Gyr (cyan). Based solely on the fit to these models, EPIC 219388192b would seem to have an age of 1 Gyr.

becomes dominant and the evolution of the stellar spin is reversed. The decay of the semimajor axis and of the eccentricity is very small because $\zeta \gg 1$, suggesting that the present eccentricity could be a remnant of the formation phase of the system.

The long timescale for the circularization of the orbit is a consequence of the small mass ratio $q \equiv M_{\mathrm{b}}/M_{\star}$ because it is inversely proportional to q when $q \ll 1$ (e.g., Equation (2) in Van Eylen et al. 2016). Therefore, it is not surprising to find such an eccentric binary system with a period of 5.29 days that is well below the circularization periods of coeval samples of stellar binaries because the latter have $q \approx 1$ (Meibom & Mathieu 2005; Milliman et al. 2014). The distribution of the eccentricities and masses of BDs in binary systems has been studied by Ma & Ge (2014) using a larger sample than that consisting only of the transiting systems that are still too few to draw firm conclusions. We refer the reader to that work for a

comparison with the distributions derived for eclipsing stellar binary and hot Jupiter systems and the interesting hints on the BD formation mechanisms that can be deduced.

The above results are weakly dependent on the value of Q'_{b}, which we assume to be 10^6 in all our calculations, because $\eta \gg 1$. The rotation of the BD is rapidly synchronized with the orbital motion within 0.1–10 Myr for a wide range of Q'_{b} (cf. Leconte et al. 2010), thus we assume it is rotating synchronously since the beginning in all our calculations.

6. Discussion and Summary

6.1. Comparison with the Baraffe et al. (2003) COND03 Models

According to the COND03 evolutionary models for cool substellar objects (Baraffe et al. 2003), a 3 Gyr old brown dwarf with a mass of $36.8\ M_{\mathrm{Jup}}$ should have a radius of $0.9015\ R_{\mathrm{Jup}}$ and a mean density of 69.71 g cm^{-3}. Our estimates of the radius and density of EPIC 219388192b are $R_b = 0.937 \pm 0.032\ R_{\mathrm{Jup}}$ and $\rho_{\mathrm{b}} = 59.6 \pm 7.6$ g cm^{-3}. They agree within 1σ with the values expected from the COND03 models. However, most of the BDs known to transit MS stars seem to be inflated (Figure 10). Commonly proposed mechanisms to explain inflated exoplanets, like their host star irradiation, tides, increased interior opacity or efficiency of the heat transfer, have little effect on brown dwarfs that are considerably more massive than exoplanets (see, e.g., Bouchy et al. 2011a, 2011b). The increase in the atmospheric opacity proposed by Burrows et al. (2007) that accounts for the slower cooling is currently thought to be mainly responsible for radius anomalies of transiting BDs. To verify this hypothesis, measurements of a secondary eclipse of EPIC 219388192b in the infrared would be highly desirable. The measurements of the secondary eclipse will allow the true temperature of EPIC 219388192b to be measured and compared with its zero-albedo equilibrium temperature ($T_{\mathrm{eq}} = 1164 \pm 40$ K) and the effective temperature expected from COND03 models (800 K). EPIC 219388192b is then also a benchmark for testing the effects of stellar irradiation. The eccentric, short-period orbit with well-known age also makes EPIC 219388192b an excellent—and unique—candidate to check the theories of star–BD tidal interactions in the presence of magnetic stellar winds (cf. Ferraz-Mello et al. 2015).

6.2. The Sample of Brown Dwarfs Transiting Main Sequence Stars

The orbital and physical parameters of the sample of known eclipsing BDs, as well as the atmospheric and physical parameters of their host stars, have been recently presented in Csizmadia (2016). EPIC 219388192b is the 13th BD found to transit a main-sequence star. With an orbital period of 5.3 days and a mass of $M_{\mathrm{b}} = 36.84 \pm 0.97\ M_{\mathrm{Jup}}$, EPIC 219388192b joins the subgroup of six short-period ($P_{\mathrm{orb}} < 100$ days) transiting BDs with masses below $\sim 45\ M_{\mathrm{Jup}}$ (Figure 11(a)). These objects are thought to have formed in the protoplanetary disk through gravitational instability (Ma & Ge 2014). The other subgroup of BDs, with masses above $\sim 45\ M_{\mathrm{Jup}}$, is believed to have formed via molecular cloud fragmentation. This group consists of seven transiting BDs, among which six have orbital periods shorter than 100 days.

The group of short-period BDs less massive than $\sim 45\ M_{\mathrm{Jup}}$ is also quite well distinguishable on the period–density diagram
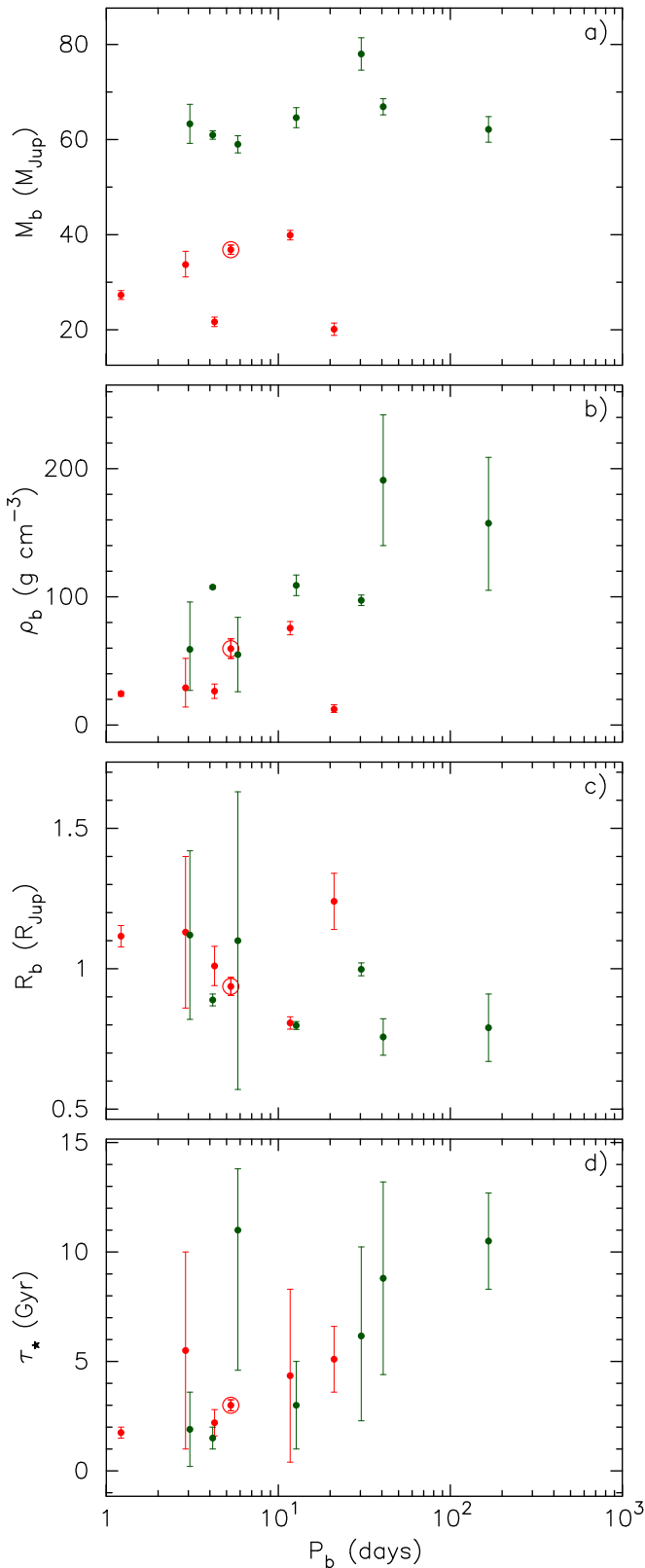
Figure 11. Period–mass, period–density, period–radius, and period–stellar age diagram for all BDs transiting MS stars. Samples and point symbols as for Figure 10.

(Figure 11(b)), as most of them have densities below 50 g cm^{-3}. With a density of 75.6 ± 5.6 g cm^{-3}, KOI-205 b (a.k.a. Kepler-492, Díaz et al. 2013) is the only object above this threshold. Two BDs more massive than $\sim$45 M_{Jup}

(CoRoT-15 b and CoRoT-33 b) have densities below 60 g cm^{-3}. These are relatively young objects (Figure 11(d)) still at the beginning of their gravitational contraction. As shown in panel (c) of Figure 11, there are only two BDs more massive than $\sim$45 M_{Jup} with radii above 1 R_{Jup}, although with large uncertainties. Most of the BDs with masses smaller than $\sim$45 M_{Jup} have radii below or very close to 1 R_{Jup}, and only KOI-205 b, with a radius of $0.807^{+0.022}_{-0.022}$ R_{Jup}, substantially differs from the rest of this group.

EPIC 219388192b is an inhabitant of the so-called "brown dwarf desert," which refers to the paucity of BD companions relative to giant exoplanets within 3 au around MS stars (Halbwachs et al. 2000; Marcy & Butler 2000). Recently, the "brown dwarf desert" was however limited only to substellar objects with the $m \sin i$ between 35 and 55 M_{Jup} and periods below 100 days (Ma & Ge 2014). This casts doubts on the proposed distinction between BDs and planets, which is thought to be connected to different formation mechanisms. Hatzes & Rauer (2015) proposed that objects in the mass range 0.3–62 M_{Jup} follow the same relationship on the observed mass–density plot, so they should be considered to belong to one and the same class of celestial objects. Based on planet population synthesis, Mordasini et al. (2009) showed that the core-accretion mechanism proposed for giant planet formation may produce planets not only more massive than 13 M_{Jup}, i.e., above the deuterium burning limit (Burrows et al. 2001), but also in the 20–40 M_{Jup}range. Based on population synthesis calculations of the tidal downsizing hypothesis, Nayakshin & Fletcher (2015) recently suggested that gravitational instability —proposed as an additional formation mechanism to the most natural one for BDs (via molecular cloud fragmentation)—can also lead to the formation of giant planets.

The ages of most of the stars known to host transiting BDs— with the exception of a few young objects—are very poorly constrained (Figure 11(d)). Any comparisons with theoretical evolutionary models, such as COND03, are therefore limited. More detections of BDs transiting stars in clusters with robust age determinations are therefore highly desirable to test substellar evolutionary models. Such detection will become possible in some of the upcoming K2 campaigns. The *TESS* and *PLATO* space missions monitor large areas of the sky. Including as many open cluster regions as possible in their programmed observations should be a high priority.

References

Asplund, M., Grevesse, N., Sauval, A. J., & Scott, P. 2009, ARA&A, 47, 481
Baraffe, I., Chabrier, G., Barman, T. S., Allard, F., & Hauschildt, P. H. 2003, A&A, 402, 701
Barnes, S. A. 2007, ApJ, 669, 1167
Barragán, O., Grziwa, S., Gandolfi, D., et al. 2016, AJ, 152, 193
Bayliss, D., Hojjatpanah, S., Santerne, A., et al. 2017, AJ, 153, 15
Béjar, V. J. S. 2011, in Proc. IX Scientific Meeting of the Spanish Astronomical Society, Highlights of Spanish Astrophysics VI, ed. M. R. Zapatero Osorio et al., 48
Bouchy, F., Bonomo, A. S., Santerne, A., et al. 2011a, A&A, 533, A83
Bouchy, F., Deleuil, M., Guillot, T., et al. 2011b, A&A, 525, A68
Bressan, A., Marigo, P., Girardi, L., et al. 2012, MNRAS, 427, 127
Bruntt, H., Basu, S., Smalley, B., et al. 2012, MNRAS, 423, 122
Buchhave, L. A., Bakos, G. Á., Hartman, J. D., et al. 2010, ApJ, 720, 1118
Burrows, A., Heng, K., & Nampaisarn, T. 2011, ApJ, 736, 47
Burrows, A., Hubbard, W. B., Lunine, J. I., & Liebert, J. 2001, RvMP, 73, 719
Burrows, A., Hubbard, W. B., Saumon, D., & Lunine, J. I. 1993, ApJ, 406, 158
Burrows, A., Hubeny, I., Budaj, J., & Hubbard, W. B. 2007, ApJ, 661, 502
Burrows, A., Marley, M., Hubbard, W. B., et al. 1997, ApJ, 491, 856
Burrows, A., Sudarsky, D., & Hubeny, I. 2006, ApJ, 640, 1063
Cardelli, J. A., Clayton, G. C., & Mathis, J. S. 1989, ApJ, 345, 245
Chabrier, G., Baraffe, I., Allard, F., & Hauschildt, P. 2000, ApJ, 542, 464
Claret, A. 2004, A&A, 424, 919
Csizmadia, S. 2016, The CoRoT Legacy Book: The Adventure of the Ultra High Precision Photometry from Space, III.6 Exploration of the Brown Dwarf Regime Around Solar-like Stars by CoRoT (Les Ulis: EDP Sciences), 143
Curtis, J. L., Wolfgang, A., Wright, J. T., Brewer, J. M., & Johnson, J. A. 2013, AJ, 145, 134
Dai, F., Winn, J. N., Yu, L., & Albrecht, S. 2017, AJ, 153, 40
Damiani, C., & Lanza, A. F. 2015, A&A, 574, A39
David, T. J., Hillenbrand, L. A., Cody, A. M., Carpenter, J. M., & Howard, A. W. 2016, ApJ, 816, 21
Dell'Omodarme, M., Valle, G., Degl'Innocenti, S., & Prada Moroni, P. G. 2012, A&A, 540, A26
Díaz, R. F., Damiani, C., Deleuil, M., et al. 2013, A&A, 551, L9
Dotter, A., Chaboyer, B., Jevremović, D., et al. 2008, ApJS, 178, 89
Doyle, A. P., Davies, G. R., Smalley, B., Chaplin, W. J., & Elsworth, Y. 2014, MNRAS, 444, 3592
Eastman, J., Siverd, R., & Gaudi, B. S. 2010, PASP, 122, 935
Ferraz-Mello, S., Tadeu dos Santos, M., Folonier, H., et al. 2015, ApJ, 807, 78

Foreman-Mackey, D., Hogg, D. W., Lang, D., & Goodman, J. 2013, PASP, 125, 306
Frandsen, S., & Lindberg, B. 1999, in Astrophysics with the NOT, FIES: A high resolution Fiber fed Echelle Spectrograph for the NOT, ed. H. Karttunen & V. Piirola, 71
Gallet, F., & Bouvier, J. 2015, A&A, 577, A98
Gandolfi, D., Alcalá, J. M., Leccia, S., et al. 2008, ApJ, 687, 1303
Gandolfi, D., Parviainen, H., Deeg, H. J., et al. 2015, A&A, 576, A11
Gaudi, B. S., & Winn, J. N. 2007, ApJ, 655, 550
Gelman, A., & Rubin, D. 1992, StaSc, 7, 457
Gray, D. F. 1992, The Observation and Analysis of Stellar Photospheres (Cambridge: Cambridge Univ. Press)
Gustafsson, B., Edvardsson, B., Eriksson, K., et al. 2008, A&A, 486, 951
Halbwachs, J. L., Arenou, F., Mayor, M., Udry, S., & Queloz, D. 2000, A&A, 355, 581
Hatzes, A. P., & Rauer, H. 2015, ApJL, 810, L25
Hauschildt, P. H., Allard, F., & Baron, E. 1999, ApJ, 512, 377
Hayano, Y., Takami, H., Oya, S., et al. 2010, Proc. SPIE, 7736, 77360N
Heiter, U., Kupka, F., van't Veer-Menneret, C., et al. 2002, A&A, 392, 619
Hirano, T., Fukui, A., Mann, A. W., et al. 2016, ApJ, 820, 41
Holmberg, J., Flynn, C., & Portinari, L. 2006, MNRAS, 367, 449
Huber, D., Bryson, S. T., Haas, M. R., et al. 2016, ApJS, 224, 2
Jenkins, J. M., Caldwell, D. A., Chandrasekaran, H., et al. 2010, ApJL, 713, L87
Kobayashi, N., Tokunaga, A. T., Terada, H., et al. 2000, Proc. SPIE, 4008, 1056
Kovács, G., Zucker, S., & Mazeh, T. 2002, A&A, 391, 369
Kreidberg, L. 2015, PASP, 127, 1161
Kupka, F., Piskunov, N., Ryabchikova, T. A., Stempels, H. C., & Weiss, W. W. 1999, A&AS, 138, 119
Leconte, J., Chabrier, G., Baraffe, I., & Levrard, B. 2010, A&A, 516, A64
Lucy, L. B., & Sweeney, M. A. 1971, AJ, 76, 544
Ma, B., & Ge, J. 2014, MNRAS, 439, 2781
Marcy, G. W., & Butler, R. P. 2000, PASP, 112, 137
Mazeh, T., Holczer, T., & Shporer, A. 2015, ApJ, 800, 142
McQuillan, A., Mazeh, T., & Aigrain, S. 2014, ApJS, 211, 24
Meibom, S., & Mathieu, R. D. 2005, ApJ, 620, 970
Milliman, K. E., Mathieu, R. D., Geller, A. M., et al. 2014, AJ, 148, 38
Mordasini, C., Alibert, Y., & Benz, W. 2009, A&A, 501, 1139
Nayakshin, S., & Fletcher, M. 2015, MNRAS, 452, 1654
Ofir, A. 2014, A&A, 561, A138
Ogilvie, G. I. 2014, ARA&A, 52, 171
Ogilvie, G. I., & Lin, D. N. C. 2007, ApJ, 661, 1180
Reffert, S., & Quirrenbach, A. 2011, A&A, 527, A140
Roeser, S., Demleitner, M., & Schilbach, E. 2010, AJ, 139, 2440
Saumon, D., & Marley, M. S. 2008, ApJ, 689, 1327
Skrzypek, N., Warren, S. J., & Faherty, J. K. 2016, A&A, 589, A49
Spada, F., Lanzafame, A. C., Lanza, A. F., Messina, S., & Collier Cameron, A. 2011, MNRAS, 416, 447
Stassun, K. G., Mathieu, R. D., & Valenti, J. A. 2006, Natur, 440, 311
Telting, J. H., Avila, G., Buchhave, L., et al. 2014, AN, 335, 41
Thoul, A. A., Bahcall, J. N., & Loeb, A. 1994, ApJ, 421, 828
Tognelli, E., Prasda Moroni, P. G., & Degl'Innocenti, S. 2011, A&A, 533, A109
Tull, R. G., MacQueen, P. J., Sneden, C., & Lambert, D. L. 1995, PASP, 107, 251
Udry, S., Mayor, M., & Queloz, D. 1999, in ASP Conf. Ser. 185, IAU Coll. 170: Precise Stellar Radial Velocities, ed. J. B. Hearnshaw & C. D. Scarfe (San Francisco, CA: ASP), 367
Van Eylen, V., Winn, J. N., & Albrecht, S. 2016, ApJ, 824, 15
Wilson, P. A., Hébrard, G., Santos, N. C., et al. 2016, A&A, 588, A144
Zacharias, N., Finch, C. T., Girard, T. M., et al. 2013, AJ, 145, 44